Howard Hughes Medical Institute

Published as: *Nat Neurosci*. 2018 November ; 21(11): 1583–1590.

Active dendritic integration and mixed neocortical network representations during an adaptive sensing behavior

Gayathri N. Ranganathan[#1], **Pierre F. Apostolides**[#1], **Mark T. Harnett**[2], **Ning-Long Xu**[3], **Shaul Druckmann**[1], and **Jeffrey C. Magee**[1,4]

[1]Howard Hughes Medical Institute, Janelia Research Campus, Ashburn, VA 20147, USA

[2]McGovern Institute for Brain Research, Massachusetts Institute of Technology, Cambridge, MA 02139, USA

[3]Institute of Neuroscience, State Key Laboratory of Neuroscience, CAS Center for Excellence in Brain Science and Intelligence Technology, Shanghai Institutes for Biological Sciences, Chinese Academy of Sciences, Shanghai 200031, China

[4]Howard Hughes Medical Institute, Baylor College of Medicine, Houston TX 77030, USA

[#] These authors contributed equally to this work.

Abstract

Animals strategically scan the environment to form an accurate perception of their surroundings. Here we investigated the neuronal representations that mediate this behavior. Ca^{2+} imaging and selective optogenetic manipulation during an active sensing task reveals that L5 pyramidal neurons in the vibrissae cortex produce a diverse and distributed representation that is required for mice to adapt their whisking motor strategy to changing sensory cues. The optogenetic perturbation degraded single-neuron selectivity and network population encoding through a selective inhibition of active dendritic integration. Together the data indicate that active dendritic integration in pyramidal neurons produces a nonlinearly mixed network representation of joint sensorimotor parameters that is used to transform sensory information into motor commands during adaptive

Correspondence to: Jeffrey C. Magee, Howard Hughes Medical Institute, Baylor College of Medicine, NRI, 1250 Moursand St, Houston TX 77030, jcmagee@bcm.edu.

Author contributions

G.R., N.X., and J.M. conceived the project and designed the experiments. G.R. performed behavioral and chronic imaging experiments and analysis. P.F.A and G.R. performed juxtacellular electrophysiology experiments and analysis. P.F.A performed slice experiments and analysis. M.H. performed whole-cell voltage recordings and analysis. G.R. and S.D performed population-encoding analyses. G.R. and J.M. wrote the paper with input from all authors.

Competing Financial Interests

The authors declare no competing financial interests.

Code availability

All data acquisition software is either commercially available (Streampix, Scanimage & Matlab) or open source (B-control & Wavesurfer). Most analysis code is commercially available as Matlab toolboxes and any analysis code that is not commercially available or already published is available from the corresponding author upon request.

A Supplementary Methods Checklist is available.

Data availability

The data that support the findings of this study are stored on Janelia Research Campus servers and are available from the corresponding author upon request.

behavior. The prevalence of the L5 cortical circuit motif suggests that this is a general circuit computation.

Introduction

Active sensing is a fundamental behavior where animals scan their environments to optimize the perception of salient objects. Examples include the orientation of the eyes for visual scene processing and the whiskers or hands for somatosensation[–]. Active sensing engages both the sensory and motor systems in concert and therefore requires a complex transformation of information from the sensory space on to motor commands and vice versa. Where and how such transformations are implemented within the mammalian nervous system remains an important area of investigation.

One powerful and general solution to this problem is for brain areas performing these computations to build a neuronal representation composed of nonlinearly mixed features that are relevant to the current environment[–]. Although evidence for such mixed representations has been reported for several cortical brain regions, their prevalence and direct link with behavior has not been established[–]. Furthermore the neuronal mechanisms involved in generating complex representations are unknown. Here, we examined these issues in layer 5 (L5) of mouse vibrissae cortex as it has been reported to possess many of the elements necessary to generate the appropriate network activity[–]. These mechanisms include an active form of dendritic integration that multiplicatively combines sensory and motor inputs in the tuft dendrites of L5 pyramidal neurons during an active sensing task in mice[–]. Such dendritic processing could therefore act as a nonlinear mixing mechanism capable of producing the type of network representation that is useful in guiding sensory-motor behavior[].

Results

Mixed selectivity in single L5 pyramidal neurons

We began by characterizing the network representation present in vibrissae cortex L5 of mice engaged in an active sensing task. We used two-photon calcium imaging from the soma/proximal apical trunk regions of L5 pyramidal neurons in head-fixed mice. The mice were trained to use a single whisker to locate an object whose position varied from trial to trial while a high-speed imaging system was used to quantify whisker related behavioral variables (Fig. 1a&b, Methods)[].

During the task, we observed Ca^{2+} signals in individual neurons that were concurrent with active whisker touches (~450–650 μm below pial surface; amplitude, 84.8±81.0 % peak $\Delta F/F$; duration, FWHM = 0.67±0.38 s, latency to first touch 124±70 ms, n = 88 neurons from 3 mice; Fig. 1c–g; see Methods). The Ca^{2+} signal amplitudes, which are proportional to neuron action potential (AP) activity (Fig S1)[–], were found to be modulated by the position of the whisker during the touch with all recorded neurons showing an elevated response for one preferred touch location (Fig 2a–c; Fig S2a&b). This was not due to differences in touch magnitude at different whisker positions (Fig S2c) and furthermore the

slope of the response-touch magnitude relationship was found to be greatest at the preferred location (preferred; 242.8±18.9, non-preferred; 35.7±4.7, n=88 neurons, $p=5.78\times10^{-20}$, two-tailed paired Student's t-test, Fig 2d–e, Fig S2d). That the slope of this relationship varies as a function of touch location indicates that response to touch is multiplicatively modulated by the position of the touch. As a result L5 neurons show a nonlinearly mixed or joint selectivity to a complex feature, sensed-object location (Fig 2f, selectivity index (SI); range: 0.9 to 2.9, mean 1.4±0.1; Fig 2g&h, Fig S2e; see Methods).

In agreement with the above Ca^{2+} imaging data, single unit (juxtacellular) electrophysiology recordings from L5 neurons (Fig 3a) revealed a similar mixed selectivity to both whisker touch and location at the time of the touch. Peri-stimulus time histograms, generated by aligning AP activity to the first touch during each behavioral trial, showed that neuronal firing rate increased with whisker touches and that the exact amount of this increase depended on object location. As with the imaging data, all individual L5 neurons expressed maximum AP firing following touches at one particular object location (Fig 3a–c, n = 17 cells from 5 mice). This effect was mirrored by an increase in the probability of burst firing evoked by whisker touches at a particular object location (Fig 3b, d), such that location preference occurred in tandem with the highest occurrence of burst firing (burst probability, preferred, 0.43 bursts/trial; non-preferred 0.24 bursts/trial, fig 3e). Again, there were no significant differences in the magnitudes of touches at the different locations (Fig 3f). These results suggest that AP burst generation substantially contributes to the mixed touched object location selectivity present in L5 pyramidal neurons of the barrel cortex.

A mixed network representation in vibrissae cortex L5

We next used Ca^{2+} imaging techniques to determine the properties of L5 network population activity during this behavior. We found that intermingled neurons often showed diverse selectivity to locations that spanned the entire anterio-posterior axis, suggesting a network with distributed representation of object location (Fig 4a&b, Fig S2f). In addition, touch-driven L5 population activity was found to accurately encode sensed-object location (see Methods) as the fraction of correct predictions obtained from a simple linear classifier was significantly above chance (Fig 4c&d, mean = 42±0.01% for pooled data, random chance = 20%, n=88 neurons, $p= 6.23\times10^{-16}$, two-sided, paired Student's t-test). L5 neurons receive inputs reflecting both absolute whisker angle (θ) and relative whisker phase (ϕ)[,,] and both could provide self-motion information that modulates the location-dependent touch response[,]. However, we found that absolute whisker angle at touch (θ_{touch}) is more informative about object location than relative whisker phase at touch (ϕ_{touch}) (Fig S3a–e) as the correlation coefficient between θ_{touch} and object location was greater than that of ϕ_{touch} and object location (r = 0.91 vs 0.32 respectively, 3315 protraction trials, 5 mice; Fig S3a). Moreover, a linear classifier could more accurately predict object location from θ_{touch} than from ϕ_{touch} (68±1% vs 27±1% correct, 20 runs, $p= 8.12\times10^{-5}$, two-sided paired Students t-test, Fig S3b shows one representative run). Notably, while both θ_{touch} and ϕ_{touch} could be predicted from recorded calcium signals as shown in Fig S3c, the prediction accuracy for θ_{touch} was 45.3±3% and the prediction accuracy for ϕ_{touch} was 27.3 ±3%. Thus, L5 neuronal output activity appears to represent the nonlinear modulation of a sensory response (whisker touch) by a motor signal (whisker angle) to generate selectivity to touch at a given location.

Altogether, the above results show that a distributed population of L5 neurons with nonlinearly mixed feature selectivity effectively encodes sensed object location, suggesting a role for this area in behaviorally relevant sensory-motor transformations.

Selective optogenetic perturbation of nonlinear mixing mechanism

To directly test the link between this network activity and active sensing behavior we developed a manipulation that would selectively target the nonlinear mixing mechanism in L5 pyramidal neurons without directly altering activity in other layers, the synaptic input to L5 or the output of L5. Because active dendritic integration of motor and sensory inputs has been reported to produce mixed feature selectivity in the distal tuft regions of these neurons, we attempted to selectively inhibit the dendritic Ca^{2+} spikes that are responsible for this multiplicative effect[9]. For this we used dispersive light activation of ArcheorhodopsinT (ArchT) directed at the cortical surface to hyperpolarize the distal tuft dendrites of L5 neurons (ArchT virally expressed in Rbp-4 cre mice, Fig S4 a–b see Methods). This manipulation effectively silenced dendritic Ca^{2+} spiking as evidenced by a large reduction in the probability and average amplitudes of global Ca^{2+} signals (probability: control; 0.37±0.04, light; 0.04±0.01, $p=5.5\times10^{-5}$, average amplitude: control; 56.6±5.9%, light; 20.9±6.2% ΔF/F, $p=5\times10^{-4}$, n=13 neurons, two-sided paired Students t-test, Fig 5a–d, Fig S4c&d). The decrease in activity was highly dependent on the initial response amplitude indicating the manipulation caused a large divisive effect on tuft activation (Fig 5c&d).

Selective silencing of the tuft also impacted L5 output activity, reducing the average Ca^{2+} signal amplitude from 54±1.4 to 34.5±0.8% ΔF/F, (n = 200 neurons, $p=3.1\times10^{-42}$, two-tailed paired Student's t-test, Fig 5e–h). Although to a lesser degree than above, a similar relationship was observed between the absolute size of the light effect and the initial amplitude of the output (Fig 5g&h), indicating that removal of tuft Ca^{2+} spikes manifests as a substantial divisive effect on neuronal output. As a control for a direct effect on output, we tested the impact of tuft hyperpolarization on neuronal output under conditions where dendritic Ca^{2+} spiking is absent even before the manipulation (Fig 5i–l). Tuft-ArchT activation under anesthesia produced only a small ~2 mV hyperpolarization of soma Vm and a ~30 pA shift in the frequency-current (F-I) curve (Fig S4h&i) that modestly reduced the firing rate by a constant ~5Hz without regard to the control firing rate (Fig 5k&l, S4j, Fig. S5). These small and uniform effects demonstrate that the manipulation does not have a substantial direct effect on the output of L5 neurons and that what effect it does have is subtractive. Instead, under normal behavioral conditions, the predominant effect of ArchT activation on neuronal output is a direct consequence of a reduction in the high frequency firing normally evoked by dendritic Ca^{2+} spiking and therefore presents as a divisive effect on neuronal output (Fig. 5m&n, Fig. S4f,g&j, Fig. S6). Thus, our manipulation appears to produce the desired inhibition of the hypothesized nonlinear mixing mechanism and its multiplicative impact on behaviorally driven L5 pyramidal neuron output with minimal off-target effects.

Effect of perturbation on network representation

We next directly assessed the impact of this manipulation on the properties of the L5 network representation (Fig 6). We found that Tuft-ArchT activation greatly lowered the

slope of response-touch magnitude relationships and the change in slope was largest at the preferred location (preferred: control 350.8±25.2, light 129.6±19.5; Non-preferred: control 95.9±8.1, light 52.3±5.3; Fig 6b&c). The manipulation also resulted in a significant reduction in the whisker touch location selectivity of L5 neurons (Fig 6a–e) that was not associated with a change in touch magnitude (Fig S7c). Ca^{2+} signal amplitudes at the preferred location were decreased to a greater extent than signals from non-preferred locations (preferred: −32.3±1.6%; non-preferred: −19.4±1.5%), causing the mean selectivity index to decrease (1.3±0.02 to 0.88±0.02; Fig 6a–f; Fig S7a, b, d). These data highlight the role of dendritically mediated gain modulation in generating touch location preference.

At the population level the manipulation flattened the mixed selectivity plots of the individual L5 neurons (Fig 6f) and it impaired L5 network encoding of sensed object location (Fig 6g) as the mean fraction of correct predictions from the linear classifier using all neurons decreased from 0.55±0.01 to 0.44±0.01 (22.7% reduction, Fig 6g, red). This effect was not likely due to a simple decrease in the average network response, as a simulated subtractive reduction using the same data did not change the fraction correct (0.55±0.01 to 0.54±0.01, 4.4% reduction, Fig 6g, green). Finally the impact on location encoding appears to be mainly driven by a reduction in the nonlinear mixing of whisker touch and whisker angle, as opposed to whisker phase and this appears to be a result of the details of the different representations (Fig S8e–h). These results indicate that active dendritic integration in individual L5 neurons mediates a nonlinear mixing of sensory-motor variables to generate a distributed population of neurons that accurately encodes the location of a sensed object. Inhibition of the nonlinear mixing mechanism by our manipulation reduced the complexity of the L5 representation to one mainly encoding only touch magnitude.

Effect of perturbation on adaptive motor behavior

We next determined the impact of degraded L5 network encoding on an active sensing behavior where mice adapt their whisking motor strategy to changes in sensory cue locations. Mice were trained to use a single whisker to locate the object which, in each trial, could occur in one of a fixed set of object locations, each location selected randomly with equal likelihood (e.g. p(loc) = 0.25 each for 4 object locations). Following training, we abruptly biased the object to occur at one particular location for a substantially larger fraction (85–90%) of trials, increasing the probability of object occurring in that location, thus moving the mean object location by ~2.5 mm (Fig 7a). Under control conditions, mice consistently responded to this change in object location by shifting their exploratory whisking to focus towards the biased object location. Mean relative whisker occupancy near the new object location increased 1.5–2 fold, and mean whisker angles shifted towards the new position by ~5° during active sampling period (Fig 7a left, 7b black; Fig S9; p=0.0047, two-sample Kolmogorov-Smirnov test; see methods for statistical analysis details). However, when a second set of mice was subjected to the above-described tuft-ArchT activation during the sampling period, they failed to show the same level of adaptation in whisking (Fig 7a right, 7b red, Fig S9; p=0.0298, two-sample Kolmogorov-Smirnov test). Since this task does not require knowledge of the object location for reward delivery, silencing global Ca^{2+} spikes did not impact the overall performance of the mice in the task

(Fig 7c, Fig S10a–e) in that the mean fraction of trials that registered false alarms (p=0.1877, Fig. S10b), the mean behavioral performance measured by the D' metric (p=0.929, Fig, S10c), average rate of rewards per number of go trials (p= 0.519, Fig, S10d) and average rate of whisker contacts per number of go trials (p=0.930, Fig, S10e) were indistinguishable when tested for statistical significance using two-sample Kolmogorov-Smirnov tests. Trimming of the whisker in well-trained mice resulted in a complete loss of performance (Fig. S10f). These results demonstrate that a reduction of active dendritic integration of sensory and motor inputs in pyramidal neurons inhibits the ability of mice to alter their whisking motor pattern in response to changing environmental sensory cues. This suggests that the sensory-motor transformations that mediate the adaptive behavior examined here require a particular network representation of sensed-object location that is formed by nonlinear mixing of different input streams within individual L5 neurons.

Discussion

In summary, we report that a specific network representation in L5 of vibrissae cortex is used (probably by downstream regions) to mediate a sensory-driven motor adaptation of whisking. This representation is composed of individual L5 neurons that each express unique selectivity for a relatively complex feature, sensed object location. We also found that a nonlinear mixing of whisker touch and whisker angular position produces this complex feature selectivity. Future experiments are required to identify the circuit elements, including the excitatory input pathways, involved in producing this neuronal selectivity. A diversity of such location selective neurons spread throughout the various columns of the vibrissae cortex could produce a basis network of neurons that encode sensed-object location independent of the whisker frame of reference (Fig S11). This type of network representation is particularly capable of supporting the coordinate transformations required for sensory-motor behaviors.

While our work points to active dendritic integration as the main nonlinear mixing mechanism generating the L5 network representation, various classes of recurrently connected networks could also contribute to, or even enhance, this computation[29,30]. However, the motor inputs carrying whisker position information predominantly arrive onto electrotonically isolated dendritic regions[7,8] and would therefore have little direct impact on neuronal output. Because of this organization active dendritic integration may be needed to first establish the mixed selectivity even before the appropriate connectivity within the recurrent network could be formed[31,32]. Together, these data suggest that active dendritic mechanisms primarily mediate the formation of the nonlinearly mixed network representation in L5 that is required for a particular aspect of sensory-motor behavior.

A recent publication reported that dendritic activation in barrel cortex L5 neurons is involved in the perception of passive (experimenter-induced) whisker movement. We, however, did not find any evidence that object detection in our active sensing based behavioral experiments requires active dendritic integration. The large differences in the tasks (active sensing versus passive movement) as well as in the specificity of some manipulations make direct comparison of these experiments difficult and may explain any discrepancies.

In terms of morphology, connectivity and physiology, the pyramidal neuron-based microcircuit motif is ubiquitous across cortical regions of the mammalian brain. In addition, there is a growing appreciation for the potential role of active dendritic processing in top-down, bottom-up input associations[,–], behavioral state modulation[], and in various forms of learning[–]. Indeed, active dendritic signals, particularly Ca^{2+} plateau potentials, provide a mechanism for behavioral experience to rapidly shape cortical representations[,], presumably in ways that improve performance. The evidence presented above suggests that, in addition to altering neuronal selectivity through plateau potential driven synaptic plasticity, these same dendritic signals also mediate a nonlinear mixing of individual features to enhance the properties of the representations. Given this, we suggest that active dendritic integration in pyramidal neurons supports a fundamental microcircuit computation, the generation of mixed-selectivity and high dimensional network representations that are readily modified by experience. Such a general computation could allow cortical areas to actively learn representations that are easily decoded and provide accurate transformations for use in adaptive behaviors. Thus, active dendritic processing in pyramidal based microcircuits underlies a fundamental computation that enables cortical areas to engage in something akin to representation learning.

METHODS

Chronic imaging window.

All procedures were carried out in accordance with protocols approved by the Janelia Research Campus Institutional Animal Care and Use Committee. All animals used in awake behaving experiments were adult (older than P60) Rbp4-cre or C57BL/6Crl mice (Charles River) crossed with appropriate reporter lines when required. During surgery, mice were anaesthetized with isoflurane (~2% by volume in O2; SurgiVet, Smiths Medical). A craniotomy (~2.5 – 3.5 mm in diameter) was made over the left barrel cortex centered at Bregma −1.45 mm, 3.25 mm lateral to midline. The dura was left intact. For experiments requiring viral injections viral vectors containing the cortex solution was slowly injected (20 nl per site, 2 to 3 sites per animal; depth ~750 μm). The GCaMP6f was expressed in layer 5 pyramidal neurons of barrel cortex in Rbp4-cre mice either by crossing transgenic reporter mice CAMKII-tTA-Ai93 mice with Rbp4-cre mice or by delivery of rAAV-syn-flex-GCaMP6f, serotype 2/1, JRC Molecular Biology), injected stereotactically into vS1 .Virus injections were made adjacent to the center of the craniotomy at 2 locations spaced ~800 μm apart and offset towards midline by ~800 μm. The injection system comprised of a pulled glass pipette (broken and beveled to 15–20 μm (outside diameter); Drummond Scientific, Wiretrol II Capillary Microdispenser) back-filled with mineral oil. A fitted plunger was inserted into the pipette and advanced to displace the contents using a manipulator (Nanoject). Retraction of the plunger was used to load the pipette with virus. The injection pipette was positioned with a Sutter MP-285 manipulator. After injection, the craniotomy was covered with a single-layered insert glass coverslip held by a donut shaped outer glass coverslip, sealed in place with dental acrylic (Jet Repair Acrylic, Lang Dental Manufacturing). The single layer insert glass was of a 177–200-μm-thickness. It was attached to a larger donut shaped glass coverslip (ID ~3mm, OD ~5 mm,) using ultraviolet cured optical adhesives (Norland Optical Adhesives 61). A titanium head-post with an

opening on the left side was attached to the skull with cyanoacrylate glue and dental acrylic to permit head fixation and two-photon imaging over the cranial window. Mice were allowed at least 5 days to recover followed by >4 days of water restriction (daily water limited to 1mL) before being head-fixed and trained at the whisker-dependent object-localization task. Distal apical dendritic tuft branches, proximal dendritic trunks, or somata of deep layer 5 neurons were imaged using a custom two-photon microscope during task performance.

Head-fixed mouse behavior.

We utilized a head-fixed active object-localization task with multiple target-object locations that require the mice to use active touch to determine the location of an object. In each trial, the target object, a vertical pole, was presented randomly at one of 5 possible 'go' positions, or at a single 'no-go' position along the anterior–posterior axis on the right side of the mice (8–9 mm lateralized from the whisker pad). The 'go' position was located within easy reach by whisking, and the location varied from trial to trial on the anterior–posterior axis, within a range of ~18 mm (~2.5 mm posterior to ~15 mm anterior to the center of the whisker pad). The 'no-go' position was in an anterior position, but within reach of the whiskers. Mice were trained to report the detection of an object at one of the 'go' positions by licking a water port, and to report an object at the 'no-go' position by withholding licking. Trained mice gradually adapted their whisker strategy and refrained from touching the object in the anterior 'no-go' location. The trial began with a delay of 1 s before the object started to ascend (time of ascent ~0.2 s) into the plane of the whiskers (Fig. 1). The object stayed in the whisker field for 1.5~2 s (the 'sampling' period) before starting to descend out of the whisker plane (time of descent ~0.3 s). This was followed by an 'answer' period (1 s) during which the mouse responds by licking or withholding licking. Licks occurring within the answer period were recorded as 'go' responses. Correct 'go' responses ('hits') were rewarded with a drop of water (~4 μl). The trial was paused for 2 s to give the mouse time to drink. Incorrect 'no-go' responses ('false alarms') led to a 'time-out' period in which the trial was paused for ~2–5 s. Licking during this time-out period triggered additional time-out periods. Correct 'no-go' responses ('correct rejections') were not rewarded. Licking outside of answer and time-out periods had no consequences. Mice refrained from licking outside the relevant periods within 2–3 sessions of training

Behavioral training began after the mice had restricted access to water for at least 5 days (1 ml per day). On days with behavioral sessions, mice generally obtained all water for the day during the session (approximately 1ml). Food was available ad libitum. The weight and health of the mice were monitored daily. After training, mice learned to respond with licking to whisker–object contact at the go- object locations.

To study sensorimotor learning (Fig 7), we designed a second phase of behavioral testing that encouraged the mice to update their whisking motor behavior in response to changing sensory cues in the form of object 'go'-locations. Following the first phase of training, we modified the likelihood of the object appearing at one of the 'go'-locations to be 0.8–0.9 and the rest of the positions together occurred for the remaining 0.2–0.1 of the trials. The rules of the behavioral paradigm were otherwise unchanged.

The behavioral apparatus was mounted under a custom two-photon microscope equipped with a high-speed whisker-imaging system, and was controlled by an open-source software system (B-control; Z. Mainen and C. Brody) running on MATLAB (Mathworks) communicating with a real-time system (TDT and RTLinux). Imaging sessions started after the mice had completed the initial training with a single whisker and reached a performance criterion of 70% correct responses or d´ > 1.5 (which typically took ~5–8 training sessions). Mice used for testing sensorimotor learning also passed this criterion.

During behavior, whiskers were illuminated with collimated light using a high- power light-emitting diode (LED) source (960 nm, Roithner) and condenser optics (Thorlabs). Images were acquired through a telecentric lens (0.36, Edmund Optics) by a high-speed complementary metal-oxide semiconductor (CMOS) camera (EoSense CL, Mikrotron) running at 500 frames per s (536 540 pixels; resolution, 24.57 pixels per mm). Image acquisition was controlled by Streampix 5 (Norpix). Synchronization of behavioral trials and two-photon imaging frames was achieved using TTL pulses sent from the real-time behavior system.

Two-photon Ca^{2+} imaging from L5 pyramidal neurons during behavior.

GCaMP6f was excited at 920 nm (typically 20–40 mW power post objective for tuft recordings and 50–70 mW for proximal trunk recordings) with a Ti:Sapphire laser (Chameleon Ultra II, Coherent) and imaged through a Nikon 16, 0.8-N.A. or a Olympus 25, 1.05 N.A objective. Emission light passed through a 565 DCXR dichroic filter (Chroma Technology) and a ET525/70m-2p filter (Chroma Technology) and was detected by a GaAsP photomultiplier tube (10770PB-40, Hamamatsu). Images (512×512 pixels) were acquired at ~30 Hz using ScanImage software.

Initial trials in a behavioral session were usually used to identify imaging fields that show visually identifiable response (corresponding to $\Delta F/F > 10\%$) during the sampling period, before a full imaging and behavior session was initiated. The location of the C2 barrel field was pre-determined using intrinsic optical imaging. In our data, ~10–20 % of dendritic trunks showed distinct touch evoked Ca^{2+} signals in > 25% trials. This is potentially an overestimation of fraction of the total L5 population, as the RbP4-cre line labeled ~70% of the L5 population. These estimates were consistent with previous studies examining active touch evoked dendritic signals.

Optogenetic silencing of L5 tuft.

For experiments to preferentially silence dendritic tuft of layer 5 neurons, floxed-ArchT driven by synapsin promoter was virally expressed by injecting AAV 2/1 carrying the floxed ArchT payload into the deep layers of barrel cortex. Ten to fourteen days after virus injection, mice began training on the tactile detection task and two-photon imaging sessions began after the criterion of 70% correct responses was reached (4–7 days after the training began). Sessions analyzed here occurred between days 5 and 32 post infection. Distal dendrites activity of deep layer 5 neurons were preferentially hyperpolarized by expressing Archaeorhodopsin-T in Rbp4-cre mice and activating the pumps with diffuse orange laser light (594 nm, Mambo laser, Cobalt, CA, USA) through the cranial window via the

objective. We used diffuse stimulation light introduced through the cranial window to activate the Arch-T pumps expressed in L5 pyramidal neurons. Pilot experiments were conducted to assess effects of light induced silencing on behavior in mice expressing Arch-T in L5 pyramidal neurons. These preliminary experiments were coupled with direct light intensity measurements above the cranial window as well as within the brain along the length of the somato-dendritic axis of the L5 population. The measurements showed that changes in whisking behavior were produced for light levels corresponding to 0.7–1.5 mW/mm^2 measured above the cranial window (viral expressing, n=2 and transgenic expression of ArchT, n=3). These light levels were adopted for use in the following experiments. The intensity of stimulation light dropped to < 20% over 500 μm of cortical depth (Fig 3a,). The light spread was calibrated to fall to negligible measures in intensity by cortical depths > 450–500 μm. Light intensity measurement were made with a custom built light meter (Applied Physics and Instrumentation Group, JRC) consisting of a glass pipette tip coated with quantum dots and couple with a fiber fed to a spectrometer. Intensity profiles were obtained through visually guided insertions of the light meter into cortical depth.

Imaging data analysis.

Lateral motion in two-photon images recorded during behavior was corrected in two steps. All frames from a behavioral session were first aligned to a target image frame using an efficient cross-correlation-based registration algorithm (single-step discrete fourier transformation (DFT) algorithm). The target image was obtained by mean projection of image frames from a trial visually identified to contain still frames. After whole-frame alignment, within-frame motion artifacts were corrected with a line-by-line registration algorithm using the gradient-descent method. To identify active branches/neurons from the image, we carried out ICA using the FastICA algorithm[,]. This routine generated independent components with hot spots matching dendritic tuft branches or apical trunks and somata that showed transients in sampled trials. The number of independent components was empirically determined such that further increases in their number extracted only noise. Regions of interest (ROIs) were manually outlined to include visually distinct hot spots. Because belonging to the same independent component does not necessarily mean belonging to the same dendritic branch or the same cell, multiple ROIs were often defined for the same independent component. This method of ROI selection was corroborated by an alternative approach using time projection of maximum value of pixel intensity above mean, $F_{max} - F_{mean}$, where F is the time series of fluorescence intensity from each pixel. For each ROI, $\Delta F/F$ (%) was calculated as $(F - F_0)/F_0$ 100, where F_0 is the mode defined from the histogram of F. ROIs with clear spatial cross-talk were visually identified and excluded from analysis. ROIs typically showed two response types, with Ca^{2+} signals occurring either during the whisker sampling epoch (during the presence of the object) or in the post-sampling epoch (after the object was removed from the whisker field, responses during this period were rare and often less reliable or consistent with time locking to observable behavioral parameters).

For the analysis of touch-related dendritic Ca^{2+} signals, only ROIs selective to sampling epoch were used. To estimate the amplitude and size of individual Ca^{2+} transients during behavioral sessions, we used a simple, absolute, threshold-driven, event-detection approach,

and measured the peak $\Delta F/F$ for Ca^{2+} events. Signals were first classified as verified Ca^{2+} events based on at least 3 consecutive point crossing threshold of 30% DF/F. From the detected events, the time point at which calcium signal crossed the fixed threshold of 30% DF/F was used to determine onset latency. For analysis of tuft dendritic signals, ROIs from the same independent components showing strong correlation with each other were treated as potentially from the same cell. A subset of these branches could be morphologically traced to belong to the same cell through imaging in z-stacks. The correlation coefficient between branches from these confirmed cells was used as criterion to determine the rest of the branches that could not be morphologically confirmed. For global Ca^{2+} signals recorded from distal tuft dendrites, neurons with at least 3 branches within the field of view were identified. Responses were deemed global Ca^{2+} spikes generated by Ca^{2+} plateaus if they were registered as events in all the branches through a threshold-crossing event detection procedure with a fixed threshold of 30% $\Delta F/F$ (> 4 s.d of average noise) (Fig 3.e). For signals recorded from dendritic trunks, ROIs rarely belonged to the same cell at the depth imaged (450 – 650 μm). Trunk signals with high correlation coefficient (>0.9) were inspected by morphological tracing if possible. ROIs traced to the same cell or belonging to the ICA with a high correlation were considered potentially belonging to the same cell, and only one of the branches was used in analysis. Whisker location preference was computed from raw Ca^{2+} signals as well as from changes in touch-force vs. response relation. Location preference measured from linear fits of signals as a function of touch magnitudes were consistent with measures from mean Ca^{2+} signals, as whisker touches were of similar magnitude ranges across all locations (Extended Data Fig 1e). Normalized selectivity in both cases was computed from response at each touch location divided by mean response under all locations. For selectivity under tuft-silenced conditions the mean was taken from the control data of the same cell collected from interleaved trials.

For testing the population encoding of object location we used a multi-class decoder based on linear discriminant analysis implemented in MATLAB (Mathworks). Population coding efficiency was quantified over 20 iterations with randomly selected data arrays of neuronal Ca^{2+} signals and the corresponding object locations from a series of touch trials. For each iteration the data arrays were randomly divided into half for training and the other half for testing. The classifier was trained with the training set and cross-validated with the testing set. Briefly, posterior probability of each test sample occurring within each of the training classes was calculated and the maximum value was used to indicate resulting class membership. We accounted for over-fitting by using lazzo regularization methods. The results of the classifier were compared with the actual object locations (θ_{touch} / ϕ_{touch}) in the test set to measure prediction accuracy. Errors were quantified by the fraction of test trials with exact prediction (predicted location = actual location). In case of tuft manipulation, data from light activated trials were used as the test set against the classifier trained with control data from the same cells in the same sessions.

Details of the method for extracting whisker variables have been described previously[11]. Briefly, whisker angle at the base of the whisker, θ, was extracted from tracked whisker trajectories. A line perpendicular to the midline was defined as θ = 0 and protraction corresponded to increasing angles. Whisking set point is the low-pass (<6 Hz) filtered whisker-angle time series [θ(t)], capturing mainly temporally averaged whisker positions.

The amplitudes of the forces in the follicle are proportional to the curvature of the whisker. We used curvature change ($\Delta\kappa$) at a particular radial location along the whisker (2–3 mm) as a proxy for the mechanical forces acting on the whiskers. Curvature was determined using a second-order polynomial fit to the whisker backbone. Automatic detection of whisker–object contact was based on a combination of minimal distance of whisker from object while thresholding $\Delta\kappa$ with the standard deviation estimated using median-absolute-deviation from frames with a minimal whisker–object distance for at least three consecutive frames (6 ms). The total curvature change during contacts, which was used as a metric for overall touch-evoked sensory drive in a given trial, was computed by summation of the absolute value of peak $\Delta\kappa$ for each contact period. Metrics for change in whisker behavior for the motor adaptation task were targeted to measure change in mean whisker position and change in time spent sampling the region in space close to the novel mean object location. Thus, changes in exploratory whisking pattern was quantified using whisker occupancy measurements. From each session, blocks of 25 trials were averaged to obtain percent whisker occupancy in the band surrounding the novel mean object position as well as the mean whisker angle. These averaged values were used to obtain a mean per-session estimate for whisker angle and percent whisker occupancy. The first two sessions without change in object location were used as baseline sessions, and whisking adaptation was measured as change from baseline in the following sessions upon switch in object location likelihood that moved the mean object location to a more anterior position. Unless otherwise indicated, data in the text are reported as mean ± s.d.

In vivo whole cell patch-clamp recording.

All animals used in this section of the study were adult male or female transgenic mice (Rbp4-cre crossed with Ai40D older than P60) expressing ArchT in L5 neurons. The level of neuronal hyperpolarization produced by light activation of ArchT was not significantly different from that produced in neurons where ArchT was expressed using viral techniques (FigS4). The animals were surgically prepared as described above for the chronic imaging experiments, with the exception of using a partial coverslip, to accommodate electrode access, as an optical window. Agarose (~1%) was applied between the dura–brain surface and the coverslip. Animals were maintained on ~1.5–2% isoflurane saturated with O_2 throughout the surgical and experimental session. The craniotomy was perfused with cortex buffer (in mM: 125NaCl, 2.5KCl, 1.2$CaCl_2$, 1.0 $MgSO_4$, 20 glucose, 20HEPES). Whole-cell current-clamp recordings were made from layer 5 pyramidal neuron somata following blind patching methods using a Dagan BVC-700 amplifier in ‘bridge’ mode, filtered at 1 kHz and digitized at 50 kHz. Pipettes had an open tip resistance of 5–8MΩ when filled with (in mM): 134K-gluconate, 6 KCl, 10 HEPES, 4 NaCl, 0.3 Tris2-GTP, 4 MgATP, 14 phosphocreatine, 0.05 Alexa 488. Pipette capacitance was neutralized just before seal formation and the bridge balance was typically 18–40 MΩ.

In vivo juxtacellular recordings.

Male C57/Bl6J mice (8–14 weeks old at the time of surgery) were implanted with a custom titanium headbar. The skull overlaying the left hemisphere remained exposed and covered with cyanoacrylic glue. Following recovery from surgery, mice were placed on water restriction (1 ml/day), all whiskers except the C-Row were trimmed and the location of the

C2 barrel was determined using intrinsic optical imaging. Behavioral training proceeded similar to the imaging experiments. Following training, a craniotomy (250–500 μm) was made over the C2 barrel and juxtacellular single-unit records were obtained from layer 5 neurons (~600–880 microns from the cortical surface) with patch-pipettes (5–10 MOhm) filled with saline. Layer 5 neurons display a diversity of responses to different sensory and non-sensory signals; as such, our strategy for this dataset was to explicitly target layer 5 neurons whose spike rate increased following touch onset. Once an individual unit was isolated, we initiated a few behavioral trials to visually determine the extent of touch-responsiveness. If the unit was deemed responsive, the recording continued until the unit was lost or the mouse stopped performing.

Spike data were online filtered at 1–5 kHz and sampled at 20 kHz. For analysis, recordings were band-pass filtered offline between 0.3–8 kHz, and spikes were identified using amplitude threshold detection. Behavioral parameters (touch onset, touch magnitude) were analyzed as described above and synchronized to electrophysiology data offline. Peri-stimulus time histograms in Figure 3b (10–30 ms bin-width) following touch onset at each pole position were generated using the nStat toolbox. Spike bursts were defined as 2 or more spikes within 300 ms of touch onset, occurring with inter-spike intervals of 10 ms or less. Black overlays on peri-stimulus time histograms are Bayesian adaptive regression fits to the data using methods described in ref 59.

In utero injection and slice electrophysiology

Pregnant Rbp4-*cre* dams were deeply anesthetized with isoflurane and embryos (E12-E14) were injected bilaterally with ~100 nL of rAAV-syn-flex-GCaMP6f or rAAV-syn-flex-ArchT-Gfp, serotype 2/1 to target layer 5 neurons. *cre*-positive pups were subsequently used at p18-p30 for slice electrophysiology. 300 μm coronal slices of the somatosensory cortex were prepared in ice-cold cutting solution containing (in mM) 28 $NaHCO_3$, 2.5 KCl, 1.25 NaH_2PO4, 7 $MgCl_2$, 0.5 $CaCl_2$, 3 pyruvate, 1 ascorbate, 7–10 glucose, and 200–215 sucrose (290–295 mOsm, saturated with 95% O_2/5% CO_2). Slices were subsequently incubated at 35 degrees C in a chamber filled with oxygenated artificial cerebrospinal fluid (ACSF) comprised of (in mM) 119 NaCl, 25 $NaHCO_3$, 3 KCl, 1.25 NaH_2PO_4, 1 $MgCl_2$, 1.3 $CaCl_2$, 3 pyruvate, 1 ascorbate, and 15–20 glucose (300–305 mOsm). Slices were subsequently kept at room temperature until use within 4 hours of preparation.

For recording, brain slices were transferred to a recording chamber and constantly perfused at 3–5 ml/min with oxygenated ACSF heated to 34 ± 1 degrees C (~1 ml chamber volume). Virus expressing neurons were targeted based on GFP or GCaMP6f expression, as visualized by 2-photon illumination (850–920 nm, Coherent Chameleon Ultra II laser). Whole-cell current clamp recordings were obtained using a Dagan BVC-700a amplifier. The patch pipette solution contained (in mM) 130 K-Gluconate, 10 KCl, 4 NaCl, 4 Mg_2-ATP, 0.3 Tris-GTP, 14 Tris-Phosphocreatine, 10 HEPES, and 0.03–0.08 Alexa-594 (~290 mOsm, [pH 7.3] with KOH). ArchT activation was achieved using full-field LED illumination (590 nm) through a 63× objective. Linescans (150–300 Hz, 12 μs laser dwell time) for GCaMP6f experiments were performed on proximal trunk dendrites with the laser wavelength set at 920 nm.

Statistical methods

No statistical methods were used to predetermine sample sizes, but our sample sizes are similar to those reported in previous publications[9]. In some cases, when data distribution was assumed, but not formally tested, to be normal, data were analyzed using two-tailed paired or unpaired *t*-tests, as stated in the text or figure legends. All manipulations were done, with control trials and trials with light administration randomly alternating. Data were analyzed automatically without consideration of trial condition. Data are shown as mean ± s.e.m. Behavioral experiments were performed blind to the experimental conditions (Arch-T+ vs Arch-T-). For the data shown in Fig. 7, the mean normalized whisker occupancy measured during sessions 3–8 were tested for differences from the normalized whisker occupancy measured during control sessions (1,2) under control and tuft-ArchT activation conditions, using Kolmogorov-Smirnov tests. For significance testing the baseline sessions of the control and tuft-ArchT activation conditions were considered similar and pooled together. The mean normalized whisker occupancies measured during sessions 3–8, from mice under baseline conditions, were significantly different from baseline measures ($p=0.0047$, two-sample Kolmogorov-Smirnov test). Whereas the mean normalized whisker occupancies measured during sessions 3–8, from mice under tuft-ArchT activation conditions, were not significantly different from the baseline measurements ($p=0.298$, two-sample Kolmogorov-Smirnov test). The normalized whisker occupancies measured in each of the sessions 3–8, from control mice and from mice under tuft-ArchT activation conditions were also compared using two-sample Kolmogorov Smirnov tests. The mean values in test sessions 3–8 that were significantly different between the two groups are indicated by asterisks in Fig. 7b (significance was considered when $p<0.01$). Normalized whisker occupancy measures from individual mice from the control group during all test sessions except session 7 were different from normalized whisker occupancy measures from individual mice under tuft-ArchT activation conditions.

Supplementary Material

Refer to Web version on PubMed Central for supplementary material.

Acknowledgements

We thank Michael Tadross and Katie Bittner for comments on the manuscript, Reza Behnam, Alla Karpova, and the Molecular Biology & Virus services at JRC for GCaMP6 and ArchT constructs; the Svoboda lab for help with software and analysis; Amy Hu and Monique Copeland for histology, Sarah Lindo for in utero surgeries and John J. Macklin for light probes. This work was supported by the Howard Hughes Medical Institute.

References

1. Yarbus AL in Eye Movements and Vision 171–211 (Springer US, 1967). doi: 10.1007/978-1-4899-5379-7_8
2. Kleinfeld D, Ahissar E & Diamond ME Active sensation: insights from the rodent vibrissa sensorimotor system. Curr Opin Neurobiol 16, 435–444 (2006). [PubMed: 16837190]
3. Cullen KE Sensory signals during active versus passive movement. Current Opinion in Neurobiology 14, 698–706 (2004). [PubMed: 15582371]
4. Mitchinson B, Martin CJ, Grant RA & Prescott TJ Feedback control in active sensing: rat exploratory whisking is modulated by environmental contact. Proc. Biol. Sci 274, 1035–1041 (2007). [PubMed: 17331893]

5. Pouget A & Snyder LH Computational approaches to sensorimotor transformations - Nature Neuroscience. Nat Neurosci 3, 1192–1198 (2000). [PubMed: 11127837]
6. Denève S & Pouget A Basis Functions for Object-Centered Representations. Neuron 37, 347–359 (2003). [PubMed: 12546828]
7. Rigotti M et al. The importance of mixed selectivity in complex cognitive tasks. Nature 497, 585–590 (2013). [PubMed: 23685452]
8. Pouget A & Sejnowski TJ Spatial Transformations in the Parietal Cortex Using Basis Functions. Journal of Cognitive Neuroscience 9, 222–237 (1997). [PubMed: 23962013]
9. Andersen RA & Snyder LH Multimodal representation of space in the posterior parietal cortex and its use in planning movements. Annual review of Neuroscience 20, 303–330 (1997).
10. Asaad WF, Rainer G & Miller EK Neural activity in the primate prefrontal cortex during associative learning. Neuron 21, 1399–1407 (1998). [PubMed: 9883732]
11. Spellman T et al. Hippocampal–prefrontal input supports spatial encoding in working memory. Nature 522, 309–314 (2015). [PubMed: 26053122]
12. Alexander AS & Nitz DA Retrosplenial cortex maps the conjunction of internal and external spaces. Nat Neurosci 18, 1143–1151 (2015). [PubMed: 26147532]
13. Barak O, Rigotti M & Fusi S The sparseness of mixed selectivity neurons controls the generalization-discrimination trade-off. J Neurosci 33, 3844–3856 (2013). [PubMed: 23447596]
14. Miller KD Canonical computations of cerebral cortex. Curr Opin Neurobiol 37, 75–84 (2016). [PubMed: 26868041]
15. Mel BW & Koch C Sigma-Pi Learning: On Radial Basis Functions and Cortical Associative Learning. 474–481 (1990).
16. Koch C & Poggio T in Multiplying with synapses and neurons (eds. McKenna TM, Davis JL & Zornetzer SF) 315–345 (1992).
17. Silver RA Neuronal arithmetic. Nat Rev Neurosci 11, 474–489 (2010). [PubMed: 20531421]
18. Harnett MT, Xu N-L, Magee JC & Williams SR Potassium Channels Control the Interaction between Active Dendritic Integration Compartments in Layer 5 Cortical Pyramidal Neurons. Neuron 79, 516–529 (2013). [PubMed: 23931999]
19. Harnett MT, Magee JC & Williams SR Distribution and Function of HCN Channels in the Apical Dendritic Tuft of Neocortical Pyramidal Neurons. Journal of Neuroscience 35, 1024–1037 (2015). [PubMed: 25609619]
20. Mao T et al. Long-range neuronal circuits underlying the interaction between sensory and motor cortex. Neuron 72, 111–123 (2011). [PubMed: 21982373]
21. Petreanu L et al. Activity in motor–sensory projections reveals distributed coding in somatosensation. Nature 489, 299–303 (2012). [PubMed: 22922646]
22. Hill DN, Curtis JC, Moore JD & Kleinfeld D Primary Motor Cortex Reports Efferent Control of Vibrissa Motion on Multiple Timescales. Neuron (2011).
23. Kleinfeld D & Deschênes M Neuronal Basis for Object Location in the Vibrissa Scanning Sensorimotor System. Neuron 72, 455–468 (2011). [PubMed: 22078505]
24. Xu N-L et al. Nonlinear dendritic integration of sensory and motor input during an active sensing task. Nature 492, 247–251 (2012). [PubMed: 23143335]
25. Chen T-W et al. Ultrasensitive fluorescent proteins for imaging neuronal activity. Nature 499, 295–300 (2013). [PubMed: 23868258]
26. O'Connor DH et al. Vibrissa-based object localization in head-fixed mice. J Neurosci 30, 1947–1967 (2010). [PubMed: 20130203]
27. Pammer L et al. The Mechanical Variables Underlying Object Localization along the Axis of the Whisker. J Neurosci 33, 6726–6741 (2013). [PubMed: 23595731]
28. Yu C, Derdikman D, Haidarliu S & Ahissar E Parallel thalamic pathways for whisking and touch signals in the rat. PLoS Biol 4, e124 (2006). [PubMed: 16605304]
29. Moore JD, Lindsay NM, Deschênes M & Kleinfeld D Vibrissa Self-Motion and Touch Are Reliably Encoded along the Same Somatosensory Pathway from Brainstem through Thalamus. PLoS Biol 13, e1002253 (2015). [PubMed: 26393890]

30. Curtis JC & Kleinfeld D Phase-to-rate transformations encode touch in cortical neurons of a scanning sensorimotor system. Nature Neuroscience 12, 492–501 (2009). [PubMed: 19270688]
31. Crochet S et al. Synaptic Mechanisms Underlying Sparse Coding of Active Touch, Neuron 69(6), 1160–1175 (2011). [PubMed: 21435560]
32. Han X et al. A high-light sensitivity optical neural silencer: development and application to optogenetic control of non-human primate cortex. Frontiers in Systems Neuroscience 5, 18 (2011). [PubMed: 21811444]
33. Salinas E & Abbott LF Coordinate transformations in the visual system: how to generate gain fields and what to compute with them. Progress in brain research (2001).
34. Salinas E & Abbott LF A model of multiplicative neural responses in parietal cortex. Proc Natl Acad Sci U S A 93, 11956–11961 (1996). [PubMed: 8876244]
35. Zipser D & Andersen RA A back-propagation programmed network that simulates response properties of a subset of posterior parietal neurons. Nature 331, 679–684 (1988). [PubMed: 3344044]
36. Buonomano DV & Maass W State-dependent computations: spatiotemporal processing in cortical networks. Nat Rev Neurosci 10, 113–125 (2009). [PubMed: 19145235]
37. Jaeger H & Haas H Harnessing nonlinearity: predicting chaotic systems and saving energy in wireless communication. Science 304, 78–80 (2004). [PubMed: 15064413]
38. Sussillo D & Abbott LF Generating coherent patterns of activity from chaotic neural networks. Neuron 63, 544–557 (2009). [PubMed: 19709635]
39. Spruston N Pyramidal neurons: dendritic structure and synaptic integration. Nature Reviews Neuroscience 9, 206–221 (2008). [PubMed: 18270515]
40. Larkum ME, Zhu JJ & Sakmann B A new cellular mechanism for coupling inputs arriving at different cortical layers. Nature 398, 338–341 (1999). [PubMed: 10192334]
41. Takahashi N, Oertner TG, Hegeman P & Larkum ME Active cortical dendrites modulate perception. Science 359, 1587–1590 (2016).
42. Bittner KC et al. Conjunctive input processing drives feature selectivity in hippocampal CA1 neurons. Nature Neuroscience 18, 1133–1142 (2015). [PubMed: 26167906]
43. Manita S et al. A Top-Down Cortical Circuit for Accurate Sensory Perception. Neuron 86, 1304–1316 (2015). [PubMed: 26004915]
44. Fu Y et al. A cortical circuit for gain control by behavioral state. Cell 156, 1139–1152 (2014). [PubMed: 24630718]
45. Zhang S et al. Long-range and local circuits for top-down modulation of visual cortex processing. Science 345, 660–665 (2014). [PubMed: 25104383]
46. Chen SX, Kim AN, Peters AJ & Komiyama T Subtype-specific plasticity of inhibitory circuits in motor cortex during motor learning. Nature Neuroscience 18, 1109–1115 (2015). [PubMed: 26098758]
47. Makino H & Komiyama T Learning enhances the relative impact of top-down processing in the visual cortex. Nature Neuroscience 18, 1116–1122 (2015). [PubMed: 26167904]
48. Xu T et al. Rapid formation and selective stabilization of synapses for enduring motor memories. Nature 462, 915–919 (2009). [PubMed: 19946267]
49. Bittner KC et al. Behavioral timescale synaptic plasticity underlies CA1 place fields. Science 357, 1033–1036 (2017). [PubMed: 28883072]
50. Khan AG et al. Distinct learning-induced changes in stimulus selectivity and interactions of GABAergic interneuron classes in visual cortex. Nature Neurosci.21, 851–859 (2018). [PubMed: 29786081]

Methods references

51. Guizar-Sicairos M, Thurman ST & Fienup JR Efficient subpixel image registration algorithms. Opt. Lett., OL 33, 156–158 (2008).
52. Greenberg DS & Kerr JN Automated correction of fast motion artifacts for two-photon imaging of awake animals. J Neurosci Methods 176, 1–15 (2009). [PubMed: 18789968]

53. Bingham E & Hyvarinen A A fast fixed-point algorithm for independent component analysis of complex valued signals. Int J Neural Syst 10, 1–8 (2000). [PubMed: 10798706]

54. Hyvarinen A & Oja E Independent component analysis: algorithms and applications. Neural Networks 13, 411–430 (2000). [PubMed: 10946390]

55. O'Connor DH, Peron SP, Huber D & Svoboda K Neural activity in barrel cortex underlying vibrissa-based object localization in mice. Neuron 67, 1048–1061 (2010). [PubMed: 20869600]

56. Clack NG et al. Automated tracking of whiskers in videos of head fixed rodents. PLoS Comput Biol 8, e1002591 (2012). [PubMed: 22792058]

57. O'Connor DH et al. Neural coding during active somatosensation revealed using illusory touch. Nat Neurosci (2013). doi:10.1038/nn.3419

58. Cajigas I, Malik WQ, Brown EN. nSTAT: Open-source neural spike train analysis toolbox for Matlab. J. Neurosci. Methods (2012). 211: 245–264 [PubMed: 22981419]

59. Ilaria Dimatteo Christopher R Genovese Robert E. Kass. Bayesian curve-fitting with free-knot splines. Biometrika (2001), 88, 1055–1071.

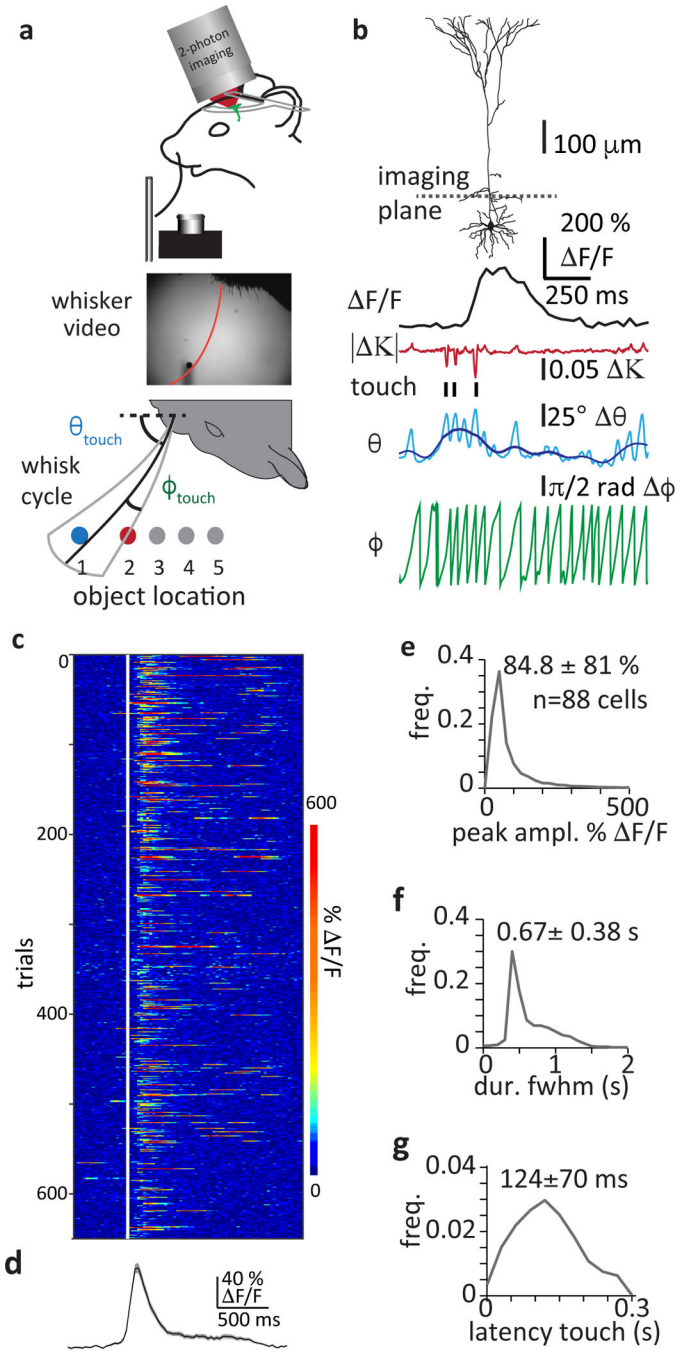

Figure 1: Layer V neuron output activity during whisker-based active sensing task.

a, Recording behavior and neuronal activity. Below, span of object location and whisking in the azimuthal plane. Two object locations (1 & 2) are highlighted (blue and red). **b**, L5 pyramidal neuron (reconstruction) with imaging plane for somatic compartment (dotted line). Below: example traces of calcium activity (ΔF/F), change in whisker curvature (|Δ**κ**|), whisker angle (θ, whisker set-point in blue) and relative whisking phase (**ϕ**) during active whisker contacts. **c**, Raster plot of touch aligned Ca^{2+} signals (white line indicates first touch) from an example neuron for an entire session. **d**, Average Ca^{2+} signal for all trials

(shaded region is SEM). **e**, Histogram of average touch evoked Ca^{2+} signal amplitudes recorded. **f**, Histogram of average duration (full width at half-max) of touch evoked Ca^{2+} signals. **g**, Histogram of average latency of Ca^{2+} signal onset to time of first whisker contact. For e-g, values shown are mean ± sem, n=88 cells.

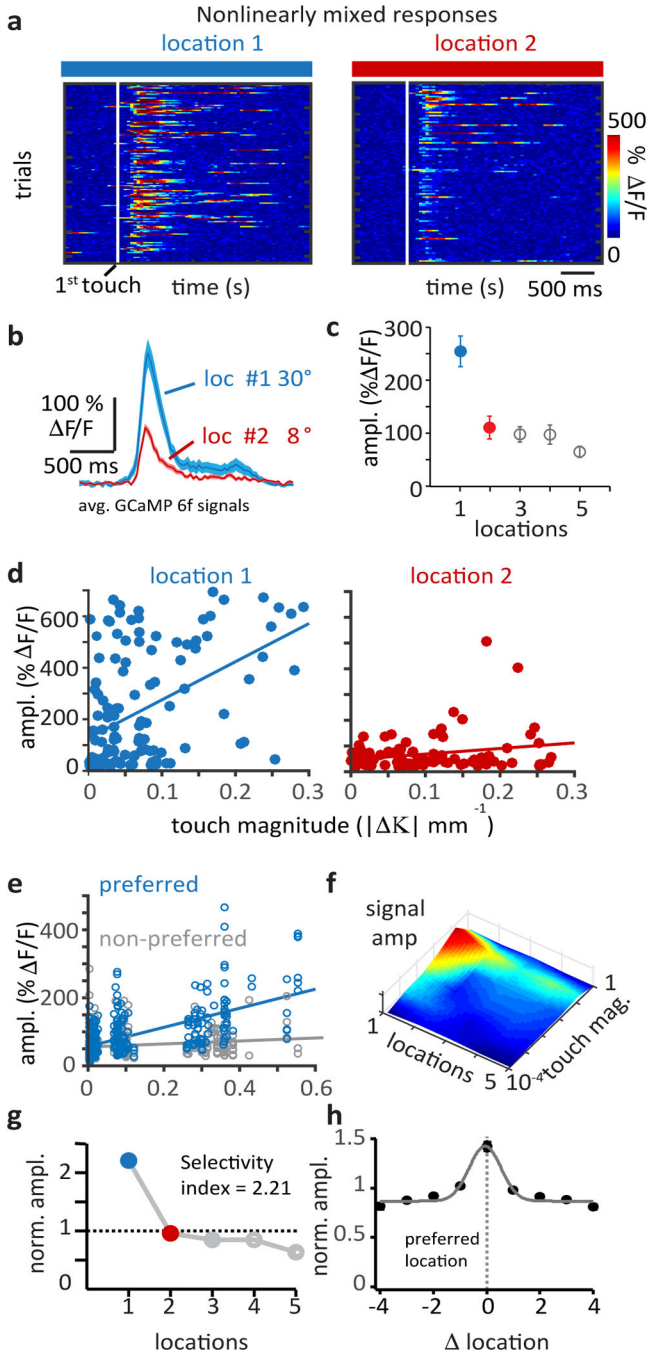

Figure 2: Nonlinear mixing of whisker touch and whisker angle produces complex feature selectivity in individual L5 neurons.

a, Raster plots of touch aligned Ca^{2+} signals (white line indicates first touch), from an example neuron, sorted into trials for pole locations 1 (blue) and 2 (red). **b**, Average Ca^{2+} signals from touch locations 1 (n=99 trials) and 2 (n=77 trials), shaded region is SEM. Whisker angle at touch indicated. **c**, Average Ca^{2+} signal amplitudes for touches at all locations, symbols are mean±sem where n=99, 77, 83, 71, 57 trials for location 1–5. **d**, Touch evoked Ca^{2+} signal amplitudes as a function of touch magnitude for touch trials at

location 1 (blue, n=99 trials) or location 2 (red, n=77 trials). Plots show nonlinearly mixed L5 activity expressed as a multiplicative joint dependence on touch magnitude and touch location. Lines are linear fits. **e**, Population data (n=88 cells) of touch evoked Ca^{2+} signal amplitudes as a function of touch magnitude for the preferred location and a single non-preferred location (location with the smallest mean Ca^{2+} signal). Touch magnitude binned. Lines are linear fits. **f**, Surface plot of mean Ca^{2+} signal amplitude as a joint function of touch magnitude and touch location from the same neuron. Amplitude scale same as panel C. **g**, Normalized Ca^{2+} signal amplitudes across touch locations and calculated mixed selectivity index showing location preference of the example neuron (location 1, blue). **h**, Normalized response amplitude as a function of location from all neurons recorded (n=88). Each cells preferred location is aligned at 0. Line shows gaussian fit. Symbols are mean ±sem where n=14,20,32,39,88,59,53,41,34 for locations −4 through +4.

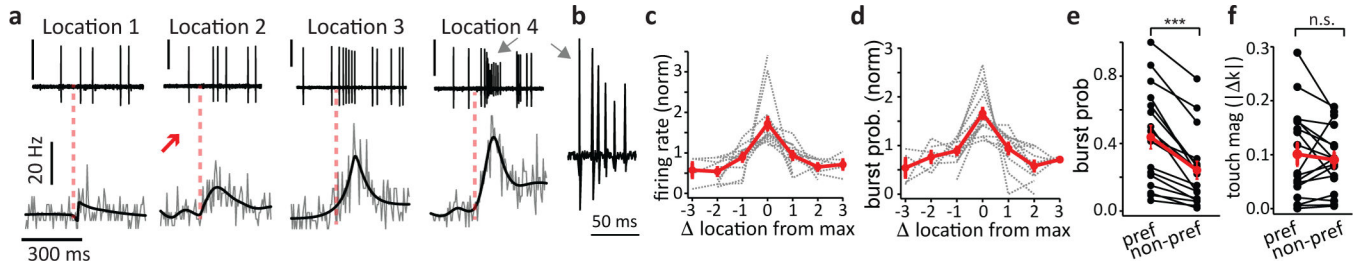

Figure 3: Contribution of high-frequency AP bursts to mixed selectivity.

a. Juxtacellular single unit recordings from layer 5 neurons in mice performing the object location task. Top row is a set of example recordings from a single cell showing spike output during a single trial at each pole location. The onset of the first whisker-pole contact indicated by the dashed red line. Gray arrows point to a high-frequency spike burst generated following the touch at location #4. Scale bar for each trace = 2 mV. Bottom row presents the average peri-stimulus time histograms corresponding to each of the four locations calculated from all trials at each location. Black overlays are Bayesian adaptive regression fits to the data (see methods). **b**. The spike burst denoted by the gray arrow in panel b is shown at an expanded time base, demonstrating the characteristics of burst firing previously shown to be driven by plateau potentials in layer 5 dendrites. **c**. Normalized firing rate following touch onset for n = 17 cells plotted as a function of distance from preferred pole location, (‘0’). Gray dashed lines are individual experiments, red is mean ± sem. **d**. Same as panel c but for normalized burst probability. **e**. Absolute burst probability at preferred and non-preferred locations. Black lines are individual experiments, red is mean ± sem. Mean burst probability at preferred location: 0.43 ± 0.07; non-preferred: 0.24 ± 0.05. p= 0.0000152, n = 17 cells from 5 mice, two-sided Wilcoxon signed rank test. **f**. Mean touch magnitude for preferred and non-preferred locations. Black lines are individual experiments, red is mean ± sem. Mean touch at preferred location: 0.100 ± 0.02; non-preferred: 0.090 ± 0.01. p = 0.45, n = 17 cells from 5 mice, two-sided Wilcoxon signed rank test.

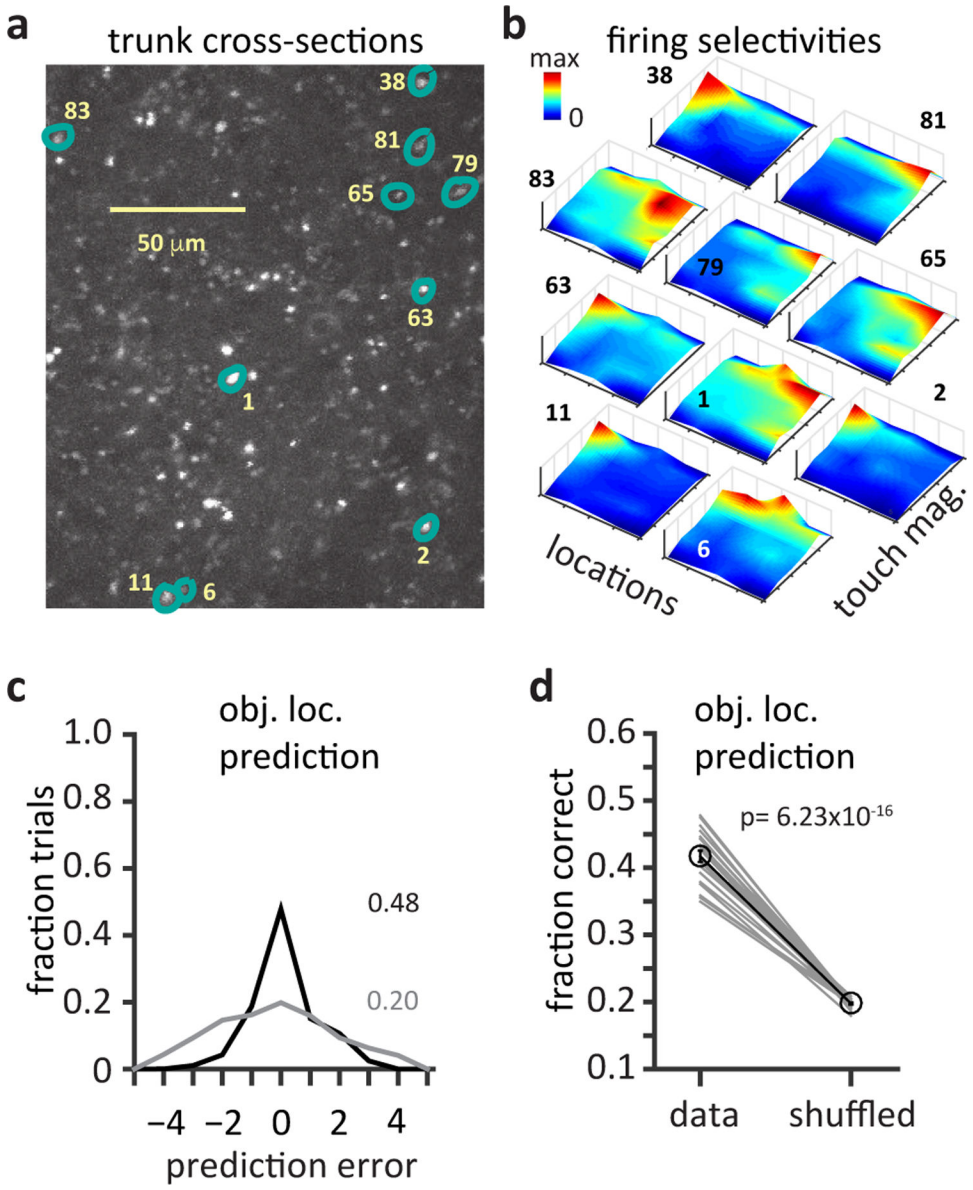

Figure 4: Diverse population of mixed selective L5 neurons generates a distributed network representation that encodes sensed-object location.

a, Image plane showing trunk cross-sections (~100 μM from soma) where output activity was recorded. **b**, Mixed selectivity maps from neurons distributed in the L5 network, numbered and highlighted in a. Surface plots show joint selectivity to combinations of touch magnitude and touch location. **c**, Prediction of touch location by a multi-class linear decoder in one iteration. The decoder was trained on half of the touch evoked Ca^{2+} responses and cross-validated on the other half. Plot shows fraction of predictions as a function of error in prediction under data aligned (black) and shuffled (green) conditions. **d**, Average accuracy in touch location prediction for 20 iterations each with random sessions recorded (n=88 neurons, 10 sessions, 3 mice). Significance tested with two-sided paired Student's *t*-test.

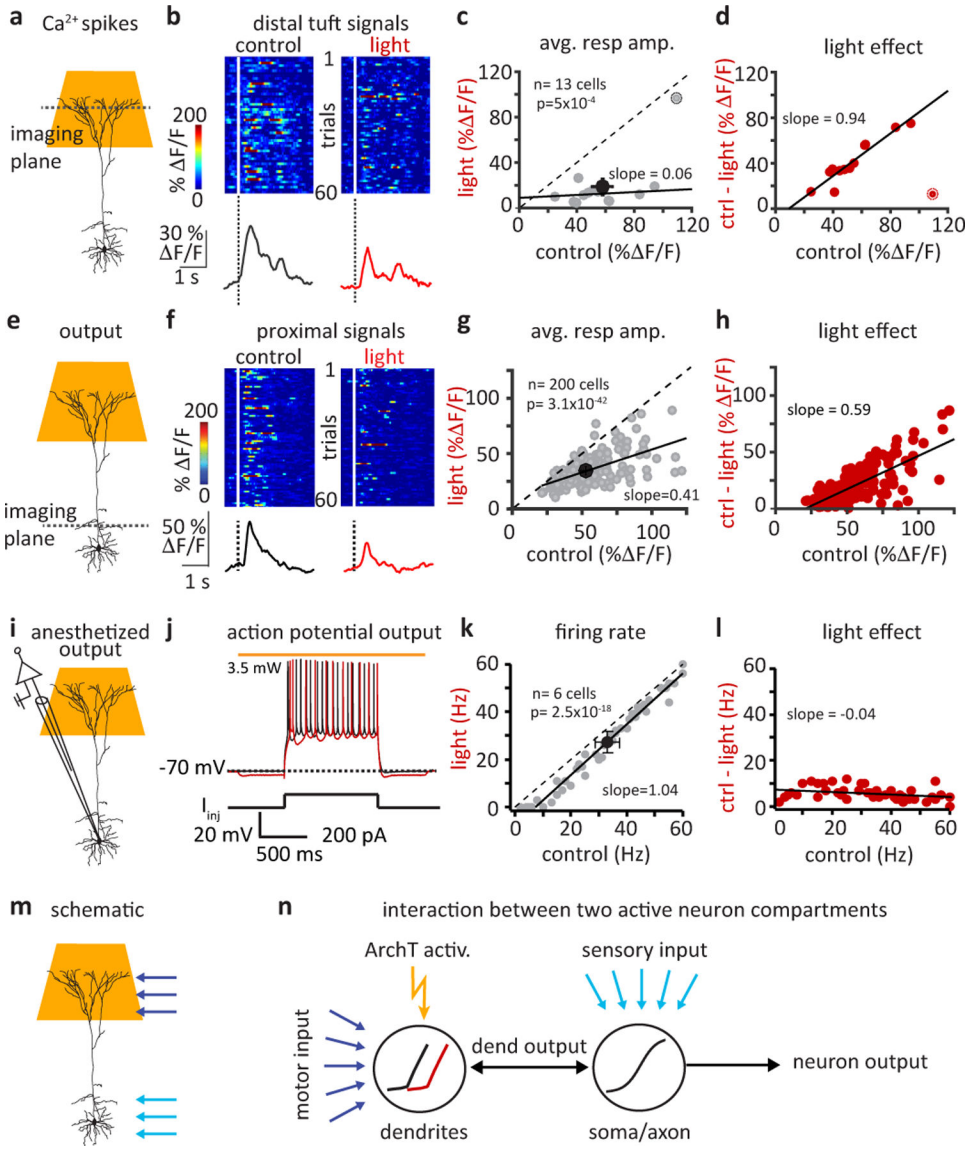

Figure 5: Optogenetic suppression of dendritic calcium spiking produces substantial divisive impact on neuronal output.

a, Schematic showing light delivery for selective silencing of L5 tuft dendrites, while imaging tuft dendrite activity. **b**, Active touch evoked Ca^{2+} signals in tuft branches. Raster plots (above) and average responses (below) are shown for responses during control (black) and light activation of tuft-ArchT (red) trials. **c**, Effect of tuft silencing on average global Ca^{2+} spike amplitudes. Gray symbols are individual cells, black symbols are mean±sem. Deviation from unity indicates a change in gain or a divisive effect. Highlighted outlier neuron not included in fit. **d**, Change in tuft Ca^{2+} response amplitude as a function of control amplitude showing a divisive effect, as the size of reduction depends on initial signal amplitude. **e**, Simultaneous tuft silencing and somatic compartment recording. **f**, Raster plots (1st 60 trials; above) and average traces (all trials; below) of Ca^{2+} events recorded under control (black) and light (red) trials. **g**, Effect of light activation on response amplitudes at the somatic compartment. Note the significant deviation from unity. Gray symbols are

individual cells, black symbols are mean±sem. **h**, Change in output response amplitude as a function of control amplitude, as in D. Note the pronounced slope indicating a divisive effect of light. **i**, Whole-cell recording set up with simultaneous tuft silencing. **j**, Example somatic Vm traces during step current injections (control; black, light; red) under anesthetized conditions devoid of active dendritic processing (light produced 2.4±0.3 mV Vm hyperpolarization; n=6). **k**, Effect of light on firing rate. Note rightward ~ 5Hz shift and not a change in slope, indicating a subtractive rather than divisive change. **l**, Change in somatic firing rate under anesthetized conditions. Comparing with d and h shows a relatively small and subtractive effect (slope ~ 0). **m**, Schematic showing predominant locations of motor (dark blue arrows) and sensory inputs (light blue arrows). **n**, Schematized interaction between two separate integrating compartments (dendrite or soma/axon) each with distinct nonlinear activation functions. ArchT activation (orange bolt) is simulated by a shift in the dendritic activation function alone (black; control, red; light). Blue arrows indicate positions of input. Black arrows indicate output of different regions. Simulation results shown in Fig S6. In this figure all statistical significance determined by two-sided paired Student's *t*-tests.

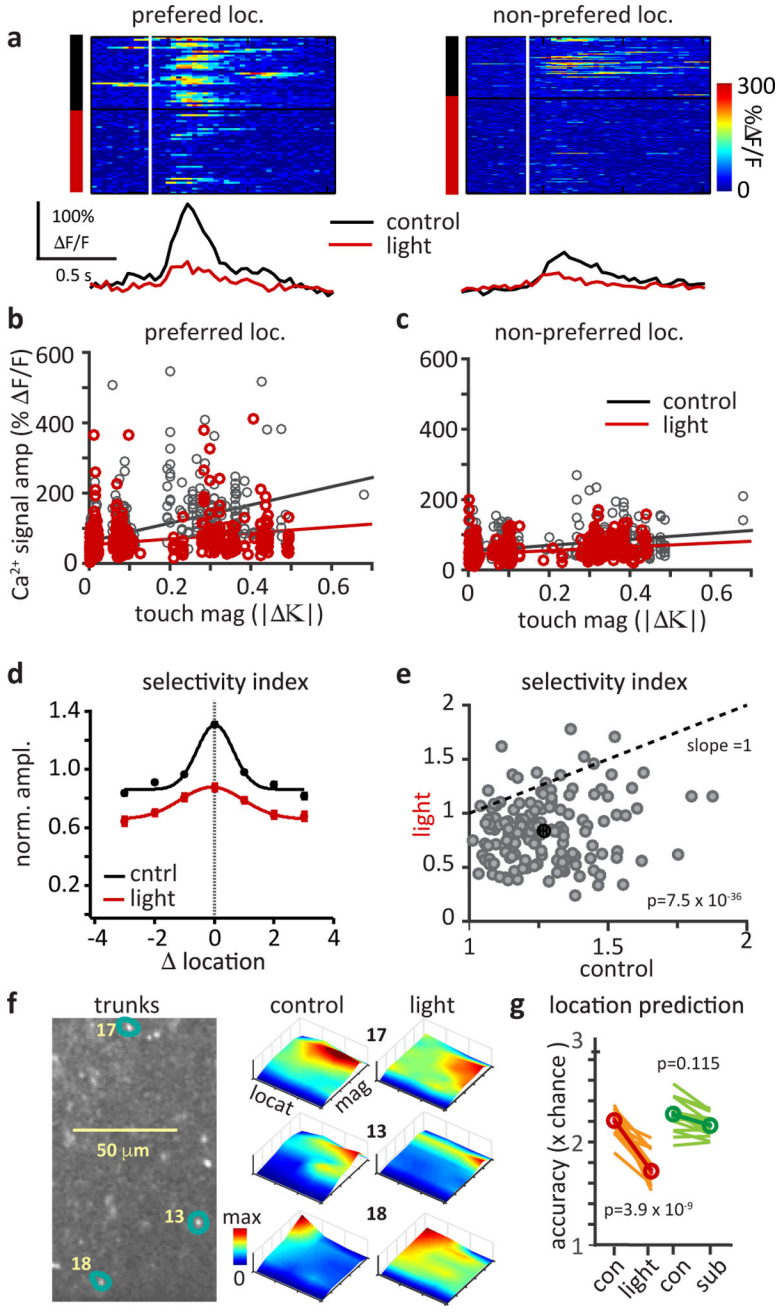

Figure 6: Selective reduction of dendritic Ca^{2+} spiking suppresses nonlinear mixing, degrading L5 network representation of sensed object location.

a, Raster plots (above) and average traces (below) of touch aligned neuronal Ca^{2+} responses sorted into control (black) and light (red) trials at the preferred (control, 36 and light, 42 trials) and a non-preferred (control, 65 and light, 106 trials) location. Mean Ca^{2+} response amplitudes binned by the touch magnitude ($|\Delta\kappa|$ for each cell at its **b**, preferred location and **c**, a non-preferred location for control (black) and light (red). Linear fits show a reduced slope, indicating a suppression of nonlinear mixed neuronal responses (reduction of slope at preferred versus non-preferred location n=152 cells, p= 2.4×10^{-18}, two-sided, paired Student's t-test). **d**, Normalized response amplitude as a function of location from all

neurons, with the preferred location of each cell aligned at 0, under control (black) and tuft-silenced (red) conditions. Lines show gaussian fits. Symbols are mean±sem where n=66, 105, 129, 200, 146, 108, 69 (black) and 64, 103, 119, 200,146, 108, 69 (red) for location −3 through +3. Comparison shows that manipulation reduces mixed selectivity. **e**, Change in location selectivity index of neurons due to light ($p=7.5X10^{-36}$, n=152 cells, two-sided paired Student's t-test). Dotted line indicates unity slope for no change. **f**, L5 apical trunk cross-sections and mixed selectivity maps for each neuron highlighted. Surface plots show joint selectivity to touch magnitude and touch location under control conditions (left) and under tuft-silenced conditions (right). **g**, Prediction of object location by a multi-class linear decoder. Lines show average effect on location prediction (expressed as × chance levels) from tuft-silencing (red) and from a simulated subtractive effect (green), n=152 neurons pooled from 10 sessions, 5 mice, $p=3.9\times10^{-9}$ (red) or p=0.115 (green) two-tailed paired Student's *t*-tests (red).

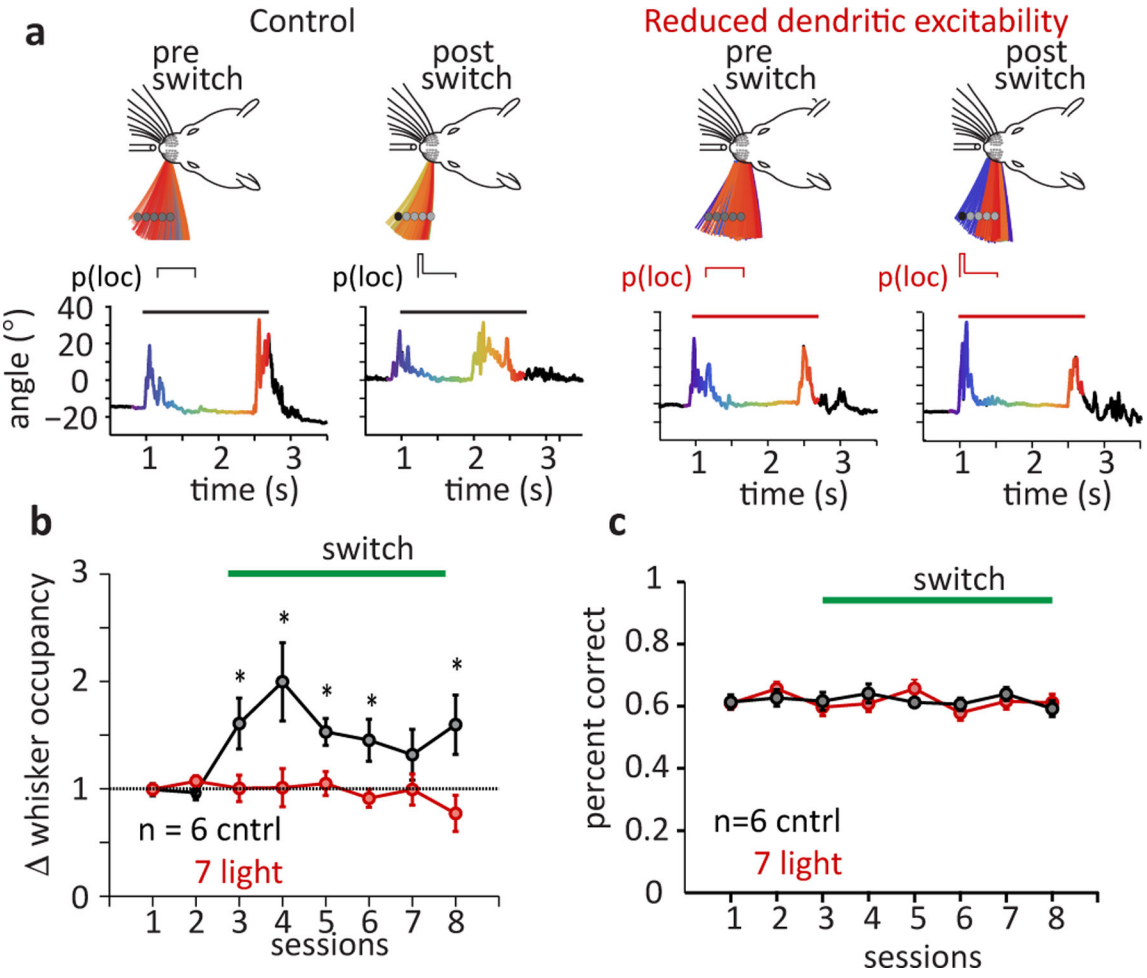

Figure 7: Selective reduction of nonlinearly mixed representation impedes adaptive whisking behavior.

a, Sensorimotor adaptation following a switch in object location and impact of silencing L5 Ca^{2+} spikes. Left panels: Example mouse, temporal evolution of the single whisker span during sampling period (above) and the associated whisker angle (below, sampling period highlighted) before and after switch in mean object location. Right panels: mouse with selective silencing of L5 tuft Ca^{2+} spikes. Colors in the whisking span and the whisker angle plots correspond to time during sampling. **b**, Normalized change in whisker occupancy following a switch in object location likelihood (at session 3) in control (black) and tuft silenced (red) mice. Asterisks indicate statistical significance (two-sample Kolmogorov-Smirnov test) between the groups where p=0.0072, 0.0033, 0.0046, 0.0051, 0.0063 for sessions 3, 4, 5, 6, 8. **c**, Average performance in object detection task during switch in object likelihood, control (black) and tuft silenced (red) mice. Error bars indicate mean±s.e.m.